



Linearized Tracking of Dendritic Evolution in Rechargeable Batteries

Asghar Aryanfar^{1,2,z} 

¹American University of Beirut, Riad El-Solh, 1107, Lebanon

²Bahcesehir University, 4 Ciragan Cad, Besiktas, Istanbul, 34349, Turkey

The formation of the dendritic microstructures during the electrodeposition is a complex process depending on several physical/chemical parameters. We establish an analytical framework for tracking the one dimensional dendritic interface based on the asynchronous developments in the concentration C and the electric potential V . Comparing the dynamics of the interface vs the ions, we establish linearized forms of the concentration C and the electric potential V during the quasi-steady-state evolution. Subsequently, we investigate the potentiostatic (V_0) and galvanostatic (i_0) conditions, where we have analytically attained the dependent parameters (i or V) and justified their respective variations in the binary electrolyte. Consequently, we have quantified the role of original concentration C_0 , the inter-electrode potential V_0 , the electrolyte diffusivity D and the inter-electrode separation l on the value and the growth rate of the dendritic interface. In particular, for the given infinitesimal dendritic growth, we have shown a higher efficacy for the electromigration than the diffusion, especially during the instigation period of the electrodeposition. © 2022 The Electrochemical Society ("ECS"). Published on behalf of ECS by IOP Publishing Limited. [DOI: [10.1149/1945-7111/ac9d6a](https://doi.org/10.1149/1945-7111/ac9d6a)]

Manuscript submitted August 5, 2022; revised manuscript received October 15, 2022. Published November 9, 2022. *This paper is part of the JES Focus Issue on Nucleation and Growth: Measurements, Processes, and Materials.*

List of Symbols

j	Ionic flux ($\text{mol.m}^{-2}.\text{s}^{-1}$)
V	Electric potential (V)
V_0	inter-electrode potential (V)
C	Concentration (mol.m^{-3})
T	Temperature (K)
ρ_{ave}	The spatial filling density ([])
D	Diffusion coefficient ($\text{m}^2.\text{s}^{-1}$)
Ω	Molar volume ($\text{m}^3.\text{mol}^{-1}$)
s	interface position (m)
\hat{s}	normalized interface position ([])
C_0	electrolyte concentration (mol.m^{-3})
C_c, C_a	cationic/anionic conc. (mol.m^{-3})
ρ_{ave}	average spatial density of dendrite ([])
ϵ_0	Vacuum Permittivity (F.m^{-1})
ϵ	Dielectric constant of electrolyte. ([])
l	Inter-electrode distance (m)
F	Faraday's constant (C.mol^{-1})
R	Universal gas constant ($\text{J.mol}^{-1}.\text{K}^{-1}$)
z	Valence electrons. ([])
i	Current density (A.m^{-2})
r, d	cell radius and diameter (m)
y	distance from growing electrode (m)
μ	mobility of moving ions ($\text{m}^2.\text{V}^{-1}.\text{s}^{-1}$)
e	electron charge (C)
N_A	Avogadro's number

The current lifestyle demands portable storage and flexible utility of energy¹ and the rechargeable batteries are one of the main and clean resources for this purpose.² The interpretation from the Moore's law is the exponential growth in the computing power, due to doubling of the the transistors every two years, which demands the increase in the source of energy and its density for portable electronics.³

One of the prominent barriers hampering the exploitation of the high-energy-density electrode materials is the non-uniform growth of the electrodeposits upon charging. The so-called *dendrites* could quickly fill substantial fraction of space with extreme porosity and

could trigger the of the short-circuit. Additionally, they can also dissolve from their thinner necks during subsequent discharge period. Such a formation-dissolution cycle is particularly prominent for the metal electrodes. Meanwhile, the metallic electrodes have a packed structure, (vs the layered structures, such as conventional graphite), therefore the upcoming ions cannot penetrate (i.e. intercalate) in depth of the electrode. Hence they keep accumulating in the surface, generating a larger cluster of the dendritic electrodeposits.⁴

In particular amongst the metals the lithium possesses the lowest volumetric density ($\rho = 0.53 \text{ g.cm}^{-3}$) and the smallest ionic radius ($r_{\text{Li}^+} = 90 \text{ pm}$) which provides a very high gravimetric energy density and possesses the highest electropositivity ($E^0 = -3.04 \text{ V}$ vs SHE) that likely provides the highest possible voltage,^{5,6} making it suitable for high-power applications such as electric vehicles.^{7,8}

Previous studies have investigated various factors on dendritic formation such as current density,⁹ electrode surface roughness,¹⁰⁻¹³ impurities,¹⁴ solvent and electrolyte chemical composition,¹⁵ electrolyte concentration,¹⁶ temperature,^{17,18} guiding scaffolds,^{19,20} capillary pressure,²¹ cathode morphology²² and mechanics.²³ Some of the recently-developed characterization techniques used include NMR²⁴ and MRI.²⁵ Recent studies also have shown the necessity of stability for solid electrolyte interphase (i.e. SEI) layer for controlling the nucleation and growth of the branched medium.^{26,27}

Dendrites instigation is rooted in the non-uniformity of electrode surface morphology at the atomic scale combined with Brownian ionic motion during electrodeposition. Any asperity in the surface is a convex-shaped peak with a high curvature that generates a large electric field and attracts the upcoming ions, acting as the electrodeposition sink for the incoming ionic flux. Indeed another significantly-contributing factor is the higher spherical diffusion in the dendritic tip relative to the flat surface.²⁸ In fact, the same mechanism is responsible for the further semi-exponential growth of dendrites in any scale. The relaxation of ionic concentration during the idle period provides a useful mechanism to achieve uniform deposition and growth during the subsequent pulse interval. Such dynamics typically occurs within the double layer (or stern layer²⁹) which is relatively small and comparable to the Debye length. In high charge rates, the ionic concentration is depleted and concentration on the depletion reaches zero;³⁰ Nonetheless, our continuum-level study extends to larger scale, beyond the double layer region.³¹

Experiment-wise, recent works have addressed the self-healing electrostatic shield,³² in situ growth of the interface,³³ optical

^zE-mail: aryanfar@caltech.edu

concentration measurement^{16,34} and the bifurcation in the growing morphology and the respective transition state.^{35–37}

Earlier model of dendrites had focused on the electric field and space charge as the main responsible mechanism³⁸ while the later models focused on ionic concentration causing the diffusion limited aggregation (DLA).^{39–41} Both mechanisms are part of the electrochemical potential,^{42,43} indicating that each could be dominant depending on the localizations of the electric potential or ionic concentration within the medium. Nevertheless, their interplay has been explored rarely, especially in continuum scale and realistic time intervals, matching scales of the experimental time and space.

The original research on the interfacial growth returns back to the analysis of the interface stability^{44,45} and exploring the spherical diffusion where the optimum interface radius for the maximum growth rate is estimated,²⁸ and later studies have complemented it via utilization of over-potential via inclusion of the curvature effect.⁴⁶ More recent works on the dendritic growth have explored the interface stability,⁴⁷ transport anisotropy,^{48,49} temperature,¹⁸ transient evolution of concentration in the dendrite tip^{39,50,51} and the larger cell domain,^{52–54} surface conduction,⁵⁵ larger-scale geometry of the electrodes,⁵⁶ cracking,⁵⁷ phase field modeling^{58–62} and effect of the elastic (mechanical) deformation.¹²

One of the main attributes of the dendrite growth, which could control the feeding rate of the ions is the solid electrolyte interphase (SEI), produced from the passivation of the electrolytic compounds on the growing interface.⁶³ Therefore, in recent developments there has been an urging need for the incorporation of its role in atomistic and continuum scales.^{64–66} Recent frameworks, has related time of the trigger of dendrites and its temperature-dependency to the surface overpotential reaching the maximum value, where the thickening of the SEI leads to the exhaust of its containing concentration of charge carriers.^{67,68}

Nevertheless the analytical understanding of the dendritic growth has yet been limited which could quantify the role of the involved parameters in the dendritic buildup.

In this paper, a new analytical development has been developed for computing the growth of the dendritic electrodeposits either during the potentiostatic or galvanostatic condition. The parametric investigation has explored the role of the original concentration C_0 , voltage V_0 , diffusivity D of the electrolyte and the current density i on the kinetics of the dendritic growth. The resulted time-dependent development is useful for design of the respective parameters suitable for avoiding the onset of the short-circuit. As well, determining the range of obtained parameters could help avoiding degradation of the electrolytic species.

Experimental

We have carried out experiments within manually-fabricated sandwich cells,⁶⁹ providing the possibility of in situ observation of the growing dendrites from their transparent separator (Fig. 1b). The cell consists of two disk Li^0 electrodes with the diameters of 1.59 cm ($r = 7.95$ mm) and the inter-electrode distance of $l = 0.32$ cm (i.e. $\frac{1}{8}$ ") housed via acrylic PMMA (i.e. Plexiglas) wall which serves as a transparent component enclosing the space between the electrodes, which provides the possibility of observation of the internally-growing microstructures. The electrolyte was synthesized via mixing the appropriate proportions of the $LiPF_6$ in the solvent with the equal volumetric ratio of ethylene carbonate and ethyl methyl carbonate (EC: EMC \equiv 1:1), generating the concentration C_0 values given in the Table I. After cell assembly, the electrolyte was filled-in via a syringe within an argon-filled and moisture-controlled glove box (H_2O , $O_2 < 0.5$ ppm). Multiple such cells were fabricated and charged with the inter-electrode potential V_0 given in the Table I, using the programmable multichannel SP150 Bio-Logic potentiostat. After each experiment, 3 images were taken from the periphery of 120° by means of Leica M205FA optical microscope through the acrylic separator, shown in the Fig. 1a. Subsequently the image processing algorithm was performed to identify the dendrites in the taken image, as below:

1. The RGB image consists of the 3 color values of $\{R, G, B\} \in [0, 255]$, where after normalizing the range of the intensity values $I_{i,j}$ will be $0 \leq I_{i,j} \leq 1$ ^a. Therefore, the grayscale image I could get computed by the weighted sum of the normalized values, using the luminosity method, as:

$$I = 0.229R + 0.587G + 0.114B \quad [1]$$

2. The grayscale image $I_{i,j}$ is binarized into $B_{i,j}$ via the grayness threshold I_c such that $J_{i,j} := 1$ if $I_{i,j} \geq I_c$ and is 0 otherwise. The threshold value I_c is attained so to minimize the weighted intra-class variance σ^2 defined proportionally as:⁷⁰

$$\sigma = \omega_0 \sigma_0^2 + \omega_1 \sigma_1^2 \quad [2]$$

where ω_0 and ω_1 are the individual weight of each portion as the fraction of total ($\omega_0 + \omega_1 = 1$) and σ_0^2 and σ_1^2 are their respective variances. Such minimization ensures that each group in the binary images are fall in the closest proximity of each other, leaving out the best binary approximation of the total grayscale image.

3. Each peripheral images on the curved boundary with the angle range of (120°) should get projected into the flat surface. From the Fig. 1b, the image width x' can get related to the central angle θ as $x' = \frac{d}{2} \sin(\theta)$, therefore the incremental width would

be $dx' = \frac{d}{2} \cos(\theta) d\theta$, where $\cos(\theta) = \sqrt{1 - \frac{4x'^2}{d^2}}$. Projecting into the realistic length δx on the boundary⁷¹ leads to $\delta x = \frac{\delta x'}{\sqrt{1 - \frac{4x'^2}{d^2}}}$,

leaving the actual length on the boundary x slightly larger than the width x' seen in the image.

4. Sweeping from left-to-right, the height of the dendrites were measured at every small segments of δx , which eventually was normalized by with respect to the inter-electrode distance ($\hat{s} := \frac{x}{l}$). The obtained fraction from total distance is a a measure for the grown dendrites, computed as:

$$\hat{s} = \frac{1}{\pi dl} \sum_{k=1}^3 \int_{-\frac{b}{2}}^{+\frac{b}{2}} \frac{\hat{s}_k(x) dx}{\sqrt{1 - \frac{4x^2}{d^2}}} \quad [3]$$

where b is the width of each image. $-\frac{b}{2} \leq x \leq \frac{b}{2}$.

Figure 1c shows such investigation for the dendritic formation in two sample images, where the red encirclement is the approximated dendrite area, the green rectangle is the total area. For each variation of electrolyte concentration C_0 and cell voltage V_0 , 3 experiments has been performed and the resulted dendrite lengths in time is shown in the Figs. 4a and 4b concurrent with the analytical results.

It is worth to mention since opening the cells for 3D imaging (tomography, etc.) will destroy the metastable dendrites, the 2D measurement of the dendrites has been performed from the periphery assuming that the in-depth (3D) pattern of formation remains in similar pattern. As well the illumination for each sample has been adjusted for the best contrast and clarity of the microstructures.

Linearized Framework

During a typical electrodeposition, the inter-electrode distance can be divided to three main compartments of the growing dendrite, the double layer (DL) and the bulk region as illustrated in the Fig. 2. The dendrite is porous medium with the thickness s which develops in time and forms a moving boundary for the bulk electrolyte, proportional to the ionic flux j . Additionally the dendrite possess the identical voltage value to the electrode, since they are physically connected. The double layer λ is where the reactions/deposition occurs⁷² and is significantly thinner relative to the inter-electrode domain l (i.e. $\lambda \ll l$). There has been a few approaches to estimate

^a i, j refer to the counter in the length and height of the image.



Figure 1. Component view (a)⁶⁹ and experimental observation (b)^{70,71} and samples of measurements (c).

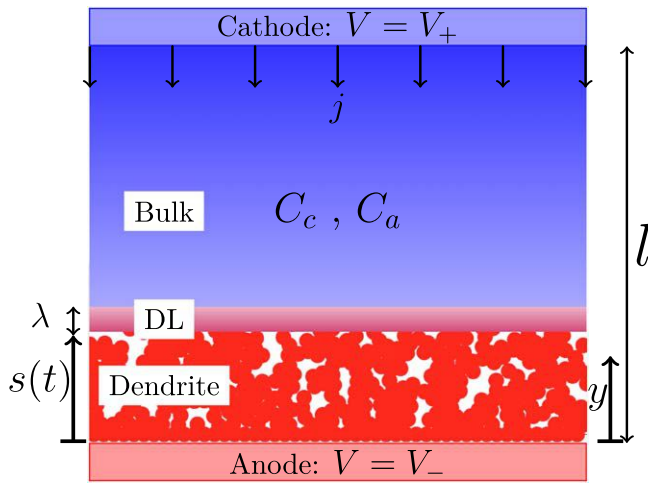


Figure 2. Schematics of 1D formation of dendrites, involving ionic concentration C_c , C_a and the respective electric potential V .

Table I. Experimental parameters (for exploring each variable, the middle value of the other parameters is considered).

Parameter	C_0	V_0	l	r	T
Value	{0.5, 1, 2}	{3.5, 4.3, 4.7}	3.175	7.95	298
Unit	M	V	mm	mm	K

the thickness of the double layer DL and herein we use the Debye length λ_D ,⁷³ which is a measure for how far the electrostatic field of a charge carrier persists:⁷⁴

$$\lambda_D \approx \sqrt{\frac{\epsilon \epsilon_0 R T}{e z^2 F C_0}} \quad [4]$$

where ϵ is the relative permittivity of the medium, ϵ_0 is the vacuum permittivity, R is the universal gas constant ($8.3 \text{ J} \cdot \text{mol}^{-1} \cdot \text{K}^{-1}$), T is the temperature, e is the electron charge, z is the number of valence electrons, F is the Faraday constant ($96 \text{ kC} \cdot \text{mol}^{-1}$) and C_0 is the ionic concentration. Needless to mention that, there has been other approaches for expressing such thin region, such as space-charge.³⁸ Finally, the bulk region, shown in the Fig. 2, is relatively a large medium for the rest of the ionic transport by means of the respective charge-carriers.

Meanwhile, the respective profiles of the concentrations C_c , C_a and the electric potential V evolve and reach the steady-state condition after an initial transition. Comparing the relatively slow

dynamics of the developing dendritic interface (i.e. $\frac{ds(t)}{dt}$) with the relatively faster variation in the aforementioned species leads to:

$$\left\{ \frac{\partial C_c}{\partial t}, \frac{\partial C_a}{\partial t}, \frac{\partial V}{\partial t} \right\} \gg \frac{ds(t)}{dt} \quad [5]$$

In fact during the growth, the ionic concentration C and electric potential V distributions have relatively reached the steady-state condition, compared to the rate of growth of the dendrites $\frac{ds(t)}{dt}$, and the micro-structural development could be approximated via merely the steady-state form of the parameters, which we refer to *quasi-steady-state* evolution.

The general governing relationship for the variation of cationic and anionic concentrations depends on the variations in the concentrations C and the electric potential V as well as the electrolyte diffusivity D and the ionic mobility μ for each ion type.^{38,50,75} Considering the quasi-steady state behavior in one dimensional progress, the Nernst-Planck relationships are simplified as below:

$$\begin{cases} D_c \frac{\partial^2 C_c}{\partial y^2} + \mu_c \frac{\partial V}{\partial y} \frac{\partial C_c}{\partial y} + \mu_c C_c \frac{\partial^2 V}{\partial y^2} \approx 0 \\ D_a \frac{\partial^2 C_a}{\partial y^2} - \mu_a \frac{\partial V}{\partial y} \frac{\partial C_a}{\partial y} - \mu_a C_a \frac{\partial^2 V}{\partial y^2} \approx 0 \\ \frac{\partial^2 V}{\partial y^2} = -\frac{e}{\epsilon \epsilon_0} (C_c - C_a) \end{cases} \quad [6]$$

In fact, the terms in the first two lines represent the role of the sole-diffusion, cooperative diffusion and electro-migration, and the sole migration. The third line additionally represents the Gauss law,⁷⁶ where the electric field is formed due to charge density. Additionally after passing through an initial transitory behavior, one can expect the system to reach the electro-neutral state where $C_c \approx C_a \approx C$. Herein we consider two distinct cases of potentiostatic ($\Delta V = V_0$) and galvanostatic ($i = i_0$) dendrite growth:

Potentiostatic dendrite growth ($\Delta V = V_0$).—During the charge, the initial uniform concentration profile C_0 gets imbalanced by the incoming/outgoing ionic flux in the oxidation/reduction sites. With the identical ionic flux j the ionic quantity should conserve, and starting from the uniform concentration of C_0 across the cell, one has:

$$\int_0^l C(y, t) dy = C_0 l \quad [7]$$

The concentration value could reach zero in the dendrite surface, when the applied potential is such large that the transport limited

Table II. Calculation parameters (For each variation the middle value of the other parameters is considered).

Parameter	Value(s)	References	Constant	Value	References
$C_0(M)$	{0.5, 1, 2}	18, 51,39	$F(\text{kC.mol}^{-1})$	96.485	77
$V_0(V)$	{3.5, 4.3, 4.7}	78–80	$R(\text{J.mol}^{-1}.\text{K}^{-1})$	8.3	81
$l(\mu\text{m})$	{25, 50, 100}	38, 82,39	$\varepsilon(l)$	80	38
$D(\mu\text{m}^2.\text{s}^{-1})$	{100, 200, 300}	16	$\varepsilon_0(\text{pF.m}^{-1})$	8.85	83
$\Omega(\text{cm}^3.\text{mol}^{-1})$	13	59,84	$N_A(\text{atom.mol}^{-1})$	6.02×10^{23}	85
$\mu(\text{nV.m}^{-1}.\text{s}^{-1})$	10	13	$\rho_{ave}(l)$	0.1	86
$i(\text{mA.cm}^{-2})$	{1, 2, 3}	16, 87,88	$\lambda(\mu\text{m})$	~ 0.14	Calculated ^{a)}

$$\begin{aligned}
 \text{a) } \lambda_D &= \sqrt{\frac{\varepsilon \varepsilon_0 R T}{e z_c^2 F C_0}} \\
 &= \sqrt{\frac{80 \times 8.85 \times 10^{-12} \times 8.3 \times 298}{1.6 \times 10^{-19} \times 9.6485 \times 10^4 \times 10^{-3} \times 6 \times 10^{23}}} \\
 &= \sqrt{1.9 \times 10^{-14}} \\
 &\approx 0.14 \mu\text{m}
 \end{aligned}$$

value for metal deposition has been reached ($j \geq j^*$). The form of the concentration profile in the bulk region previously has been expressed either as a straight line³⁹ or with a slight positive curvature³⁸ and Fig. 3a visualizes the linearization where the concentration profile starts from the growing dendrite interface and extending from the double-layer and bulk region, reaching the counter-electrode. The form of the profile is obtained as:

$$C(y, t) \approx \begin{cases} 0 & 0 \leq y < s(t) \\ \frac{2C_0 l}{(l - s(t))^2} (y - s(t)) & s(t) \leq y < l \end{cases} \quad [8]$$

where the coefficient of linear profile $\left(\frac{2C_0 l}{(l - s)^2}\right)$ is obtained by the ionic conservation given in the Eq. 7.

Considering the electroneutrality, one expects the voltage profile to be linear segments based on the third line in the Eq. 6. Figure 3b represents the voltage profile across the cell, where the largest variation occurs in the double-layer region with the scale of Debye length λ ^{38,39} and has been linearized as a straight line as:

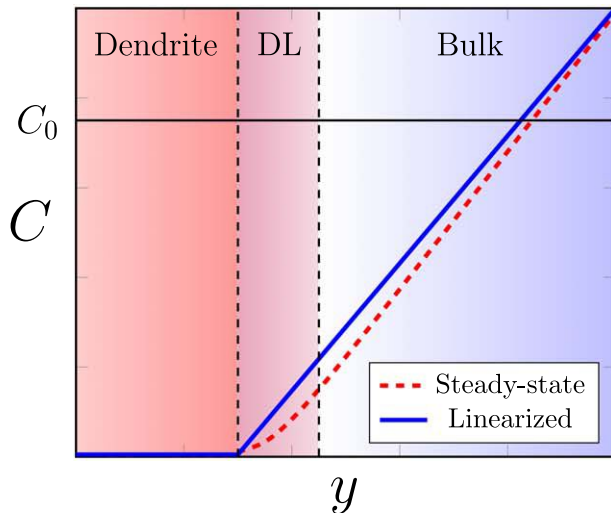
$$V(y, t) \approx \begin{cases} 0 & 0 \leq y < s(t) \\ \frac{V_0}{\lambda} (y - s(t)) & s(t) \leq y < s(t) + \lambda \\ V_0 & s(t) + \lambda \leq y < l \end{cases} \quad [9]$$

The dendritic microstructure develops based on the feeding ionic density j in the interface, inside the double layer region, as:

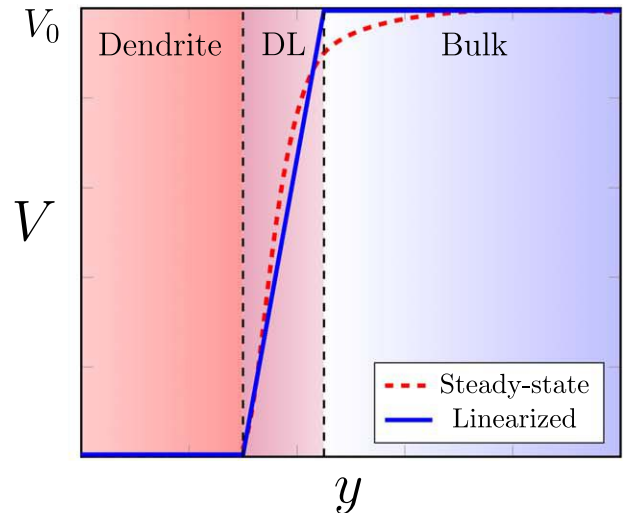
$$\frac{ds(t)}{dt} \approx -\frac{\Omega}{\rho_{ave}} j \quad [10]$$

where Ω is the molar volume of the dendritic material, ρ_{ave} is the average spatial density of the dendrite, which additionally have been approximated to be constant during the one dimensional growth. In fact the evolution of the dendrites has been found to start with an initial formation of dense electrodeposits, followed by a branched morphology pattern, with the average density of ρ_{ave} ,^{35,36} which depends on the material type, charging conditions, electrolyte composition, etc.

The ionic flux j is obtained cooperatively from the gradients of concentration C and the voltage V as:³⁸



(a) Linearized concentration profile.



(b) Linearized voltage profile.

Figure 3. The simplified form of the profiles during the dendritic evolution, with the exaggerated double layer thickness λ .

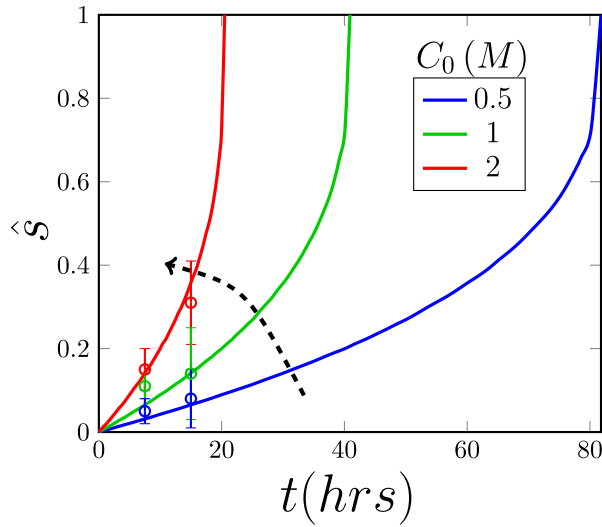
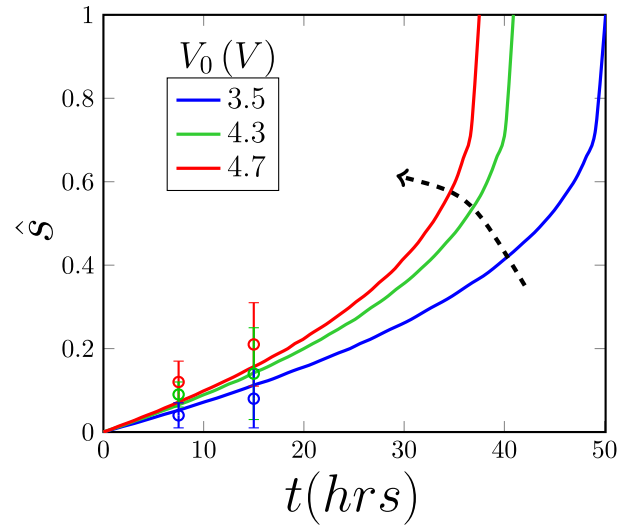

 (a) Dendritic interface s vs the original concentration C_0 .

 (b) Dendritic interface s vs the original potential V_0 .

Figure 4. The role of original concentration C_0 and voltage V_0 on the progress of the dendritic interface. The experimental values are additionally illustrated with their respective standard deviation.

$$j = -D \frac{dC_c}{dy} - \mu_c C_c \frac{dV}{dy} \quad [11]$$

where the negative sign shows that the direction of ionic flux j is in the opposite of the concentration and voltage gradients. Combining Eqs. 11, 10, 8 and 9 leads to:

$$\frac{ds(t)}{dt} = \frac{2\Omega C_0 l}{\rho_{ave}(l-s)^2} \left(D + \frac{\mu V_0}{\lambda}(y-s) \right) \quad [12]$$

where the rearranging leads to the time-dependency of the dendrite scale s :

$$\frac{(l-s(t))^2 ds(t)}{D + \frac{\mu V_0}{\lambda}(y-s)} = \frac{2\Omega C_0 l}{\rho_{ave}} dt \quad [13]$$

The extra variable y in this equation is relatable to the dendrite scale $s(t)$. The double layer region typically shields the growing

interface, where $y \in [s(t), s(t) + \lambda]$ and is a substantially thinner range relative to the inter-electrode domain ($\lambda \ll l$). Hence one can approximate it as $y \approx s(t) + \frac{\lambda}{2}$, which leads to:

$$\int_0^{s(t)} \frac{(l-s(t))^2}{D + \frac{\mu V_0}{2}} ds(t) \approx \int_0^t \frac{2\Omega C_0 l}{\rho_{ave}} dt \quad [14]$$

therefore, the integration leads to:

$$s(t) \approx l - \sqrt[3]{l^3 - \frac{6\Omega C_0 l}{\rho_{ave}} \left(D + \frac{\mu V_0}{2} \right) t} \quad [15]$$

The analytical relationship in the Eq. 15 opens room for the investigation of the individual parameters on the dendrite growth. Exploiting the literature values given in the Table II, Figs. 4a, 4b, 5b and 5a show the role of original concentration C_0 , original inter-electrode potential V_0 , the inter-electrode distance l and the diffusion

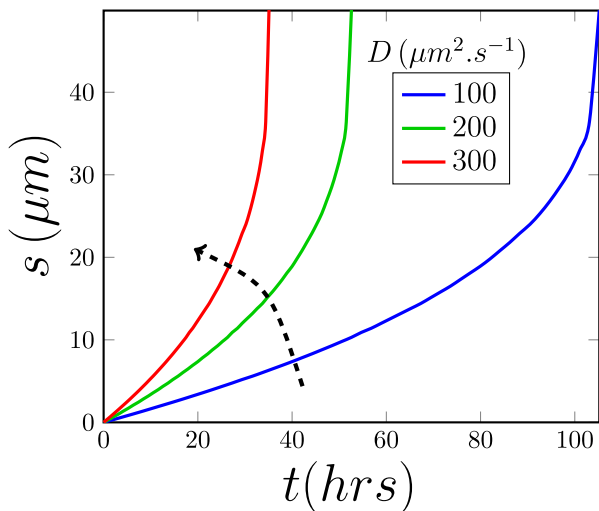
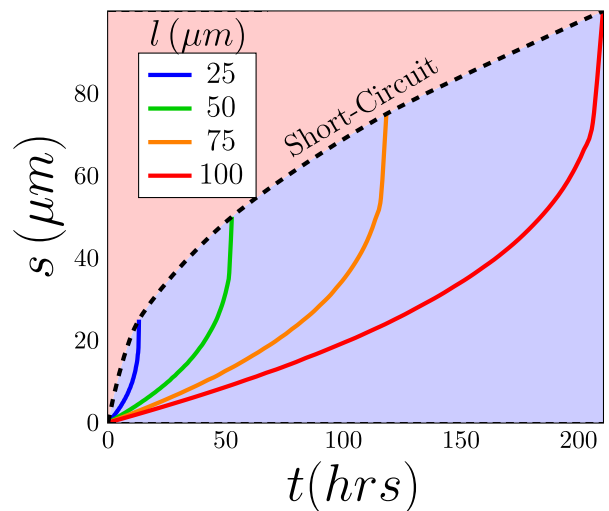

 (a) Dendritic interface s vs the diffusivity D .

 (b) Dendritic interface s vs the scale of the electrochemical cell l .

Figure 5. The role of cell scale l and the diffusion coefficient D of the electrolyte.

coefficient D of the electrolyte on the real-time evolution of the dendrite scale $s(t)$.

Consequently, the short-circuit time t_{short} could be analytically obtained by setting $s(t_{\text{short}}) := l$ as:

$$t_{\text{short}} = \frac{\rho_{\text{ave}} l^2}{6\Omega C_0 \left(D + \frac{\mu V_0}{2} \right)} \quad [16]$$

Galvanostatic dendrite growth ($i = i_0$).—For the galvanostatic case, the mass balance Eq. 10 can easily be integrated to:

$$s(t) = \frac{C_0 \Omega j_0 t}{\rho_{\text{ave}}} \quad [17]$$

where $j_0 = \frac{i_0}{zF}$ is the respective constant ionic flux during the galvanostatic development. The short-circuit time simply obtained as:

$$t_{\text{short}} = \frac{\rho_{\text{ave}} l}{C_0 \Omega j_0} \quad [18]$$

The ionic flux j_0 is in fact generated either due to the gradients of the concentration C or the electric potential V (Eq. 11) and one can compute the evolution of the voltage profile $V(y)$ as:

$$j_0 = D \frac{2C_0 l}{(l - s(t))^2} + \mu \frac{2C_0 l}{(l - s(t))^2} \times (y - s(t)) \frac{dV}{dy} \quad [19]$$

One notices that in the interface of the dendrite with the electrolyte $y = s$ the voltage dependency second term in the *RHS* vanishes and the only remaining response for the flux becomes diffusion (first term). Therefore, in order to find the voltage profile in the Bulk medium (a shown in the Fig. 2), since the double-layer region is substantially thin region ($\lambda \ll l$), we move forward with setting the integral boundary to $y \in \left[s(t) + \frac{\lambda}{2}, l \right]$. Re-arranging gives the following approximation:

$$\int_{s+\frac{\lambda}{2}}^y \frac{dy}{y - s(t)} \approx \int_0^V \frac{\mu dV}{\frac{(l - s(t))^2}{2C_0 l} j_0 - D} \quad [20]$$

which can get integrated to extract the electric potential $V(y)$ profiles as:

$$V(y) \approx \left(\frac{(l - s(t))^2 j_0}{2C_0 l \mu} - \frac{D}{\mu} \right) \ln \left(\frac{y - s(t)}{\lambda} \right) \quad [21]$$

which is valid in the range of $y \in \left[s(t) + \frac{\lambda}{2}, l \right]$. The galvanostatic voltage profile $V(y)$ vs the distance in the bulk region is illustrated for different current densities in the Fig. 6b.

Results and Discussion

The linearization of the concentration C and electric potential V profiles in the Eqs. 9 and 8 in fact quarantines their respective second derivative to tend to zero, which verifies the steady-state approximations in the Nernst-Planck relationships (Eq. 6) for the most part, except the middle term in the double layer region, which could get approached by:

$$\mu_c \frac{\partial V}{\partial y} \frac{\partial C_c}{\partial y} \sim \frac{2\mu_c C_0 V_0}{\lambda l^2} \quad [22]$$

Therefore, in order for the approximations to be valid one should have low concentration ($C_0 \rightarrow 0$) or low voltage ($V_0 \rightarrow 0$) regimes of operation.

The original assumption of the concentration profile in the Eq. 8 is to start from zero value in the dendrite interface ($C(s) = 0$). This could occur via imposing high-enough current (or voltage) which previously has been estimated as:⁸⁷

$$i^* = \frac{2DC_0 zF}{l} \frac{\mu_a + \mu_c}{\mu_a} \sim 1 \frac{A}{m^2} \quad [23]$$

since the value of the order of the current densities considered in the Table II, the assumption are valid. Additionally, the quasi-steady assumptions in the Eq. 6 could be investigated by calculating the transition time for vanishing the concentration in the electrode which is known as the Sand's time t_{Sand} as:⁸⁹

$$t_{\text{Sand}} = \pi D \left(\frac{C_0}{2j} \right)^2 \left(\frac{\mu_a + \mu_c}{\mu_a} \right)^2 \sim 1s \ll t_{\text{Dendrite}} \quad [24]$$

where μ_a and μ_c are the respective cationic and anionic mobilities. Since the transition time t_{Sand} is almost negligible relative to the dendrite life time, therefore the growth occurs almost entirely in the quasi steady-state regime and such assumption proves to be valid. Nonetheless, the Sand's time, which was originally developed from classical diffusion equation,⁹⁰ could get complemented via inclusion of additional involved factors, such as solid electrolyte interface (SEI),⁹¹ which leads to even smaller values for the instigation of dendritic morphology and is consistent with the current analogy in the Eq. 24.

The dendritic run-away behavior obtained in the Figs. 4b, 4a, 5b and 5a in fact is due to the augmentation in the electric field E due to progress of the dendrite interface and the decrease in the remaining bulk medium. This resembles with the previously well-known relationship for the progress speed of the dendritic interface as:^{92,93}

$$v = \mu_a E \quad [25]$$

which mentions that the speed of the growing interface is the same as the speed of the escaping anions from the interface due to migration.^{93,94} From the Eq. 25, assuming one dimensional growth pattern with negligible interface curvature we arrive at the following for the potentiostatic case:

$$\frac{ds}{dt} \approx \mu_a \frac{V_0}{l - s} \quad [26]$$

therefore, re-arranging gives:

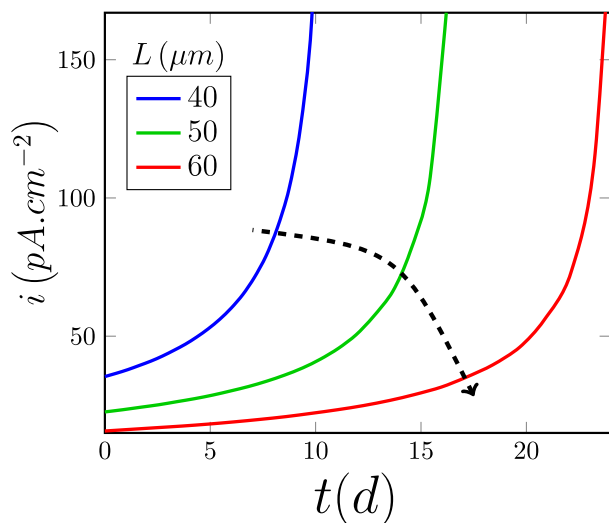
$$\int_0^s (l - s) ds \approx \int_0^t \mu_a V_0 dt \quad [27]$$

and integrating leads to:

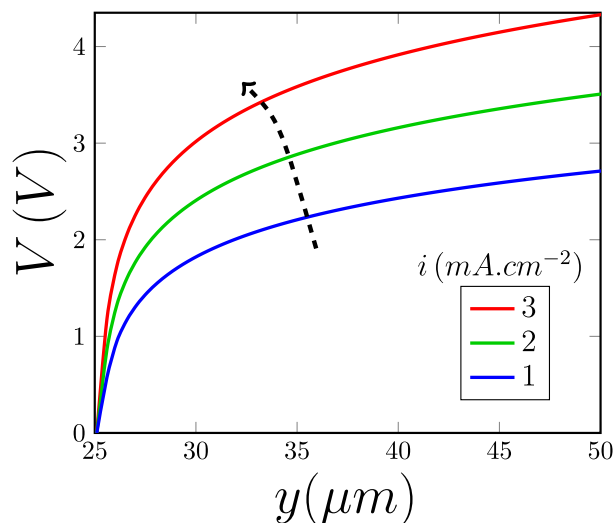
$$s(t) \approx l - \sqrt{l^2 - 2\mu_a V_0 t} \quad [28]$$

This relationship in fact highly resonates with the quickening trend represented in the Eq. 15. Additionally, the parameter-wise variations obtained in the Figs. 4a, 4b and 5a are intuitively obvious, since the increase either in the initial concentration C_0 , voltage V_0 , electrolyte diffusivity D would exacerbate the run-away behavior in the dendritic development. The trend in the Fig. 5b additionally has inverse relationship with the dendritic growth, since higher scale l leads to lower electric field E , leading to decrease in the dendritic development.

While both potentiostatic ($\Delta V = V_0$) and galvanostatic ($i = i_0$) forms of interface progress have been explored separately, the



(a) The current density $i(t)$ during potentiostatic charging ($\Delta V = V_0$).



(b) The evolution of voltage profile $V(y)$ during the galvanostatic charging ($i := i_0$) for half-way dendrite progress ($s := 0.5l$).

Figure 6. Tracking of the variable parameters (current in potentiostatic method and voltage in galvanostatic method) during the two forms of charging.

remaining parameter can be tracked which is roughly related to the Ohm's law.⁷⁶ For the potentiostatic case, one can get the current density i via reverting back from time-derivative of the Eq. 10 as:

$$i = \frac{\frac{2\Omega C_0 l}{\rho_{ave}} \left(D + \frac{\mu V_0}{2} \right)}{\sqrt[3]{\left(l^3 - \frac{6\Omega C_0 l}{\rho_{ave}} \left(D + \frac{\mu V_0}{2} \right) t \right)^2}} \quad [29]$$

Figure 6a visualizes the current density evolution which shows a run-away behavior of the current density i vs time t . As well for the galvanostatic case, the build up of the voltage V with the logarithmic form in fact in match with the long term form of the voltage profile illustrated in the Monroe & Newman.³⁹

Having a closer look at the analytical relationship given in the Eq. 15 the coefficients of D and $\frac{\mu_0 V}{2}$ are individually responsible for the role of diffusion and electromigration. If the δs_{Diff} and sole δs_{Mig} illustrate their individual displacements from either effect, one has:

$$\begin{aligned} \frac{\delta s_{\text{Diff}}}{\delta s_{\text{Mig}}} &= \frac{\frac{\partial s}{\partial D}}{\frac{\partial s}{\partial \left(\frac{\mu_0 V}{2} \right)}} = \frac{2D}{\mu V_0} \left(\frac{l^3 - 3\beta \frac{\mu V_0}{2} t}{l^3 - 3\beta D t} \right)^{\frac{2}{3}} \\ &\ll \frac{2D}{\mu V_0} = \frac{2\mu k_B T}{\mu V_0} \ll 1 \end{aligned} \quad [30]$$

Where $\beta := \frac{2\Omega C_0 l}{\rho_{ave}}$ is a coefficient with the unit of m , and the relationship between the diffusivity D and mobility μ is obtained from the Einstein relationship as $D = \frac{\mu k_B T}{e}$. The obtained equation shows a significantly higher efficacy of the electromigration relative to the diffusion on the current density i and ultimately the dendrite scale $s(t)$. This is particularly obvious during the instigation of the electrodeposition, since initially the free ions have uniform distribution with no gradient, and the remaining sole drive for the ionic flux is the difference in the electric potential (i.e. electromigration).

Needless to mention that the obtained profiles for the concentration C and voltage V considers the wholistic view of the dendritic

growth in the simple form and extra complexities such as SEI or the chemical composition of the electrolyte. In fact such consideration in the model will add.

Conclusions

In this paper we have developed an analytical method for the evolution of the dendritic electrodeposits via considering the linearized transition in the profiles of ionic concentration C and the electric potential V which we refer as quasi steady-state development. Considering two distinct methods of potentiostatic (V_0) and galvanostatic (i_0) dendritic growth, the Ohm's law-based dependent parameter (i or V) is analytically obtained and justified. We have additionally explored the role of the potential V_0 , initial concentration C_0 , diffusion coefficient D and domain scale l on the rate of the dendritic development. The established relationship can be utilized for the design process of the range of the parameters for preventing the short circuit as well as the possible electrolyte degradation.

Acknowledgments

The author would like to thank and recognize the support from Masri Institute for energy and sustainability at American University of Beirut, Award #103919. The authors declare that they have no competing financial interests to influence the work reported in this paper. The raw data for producing the results in this manuscript are freely available upon request from the corresponding author at aryanfar@caltech.edu.

ORCID

Asghar Aryanfar  <https://orcid.org/0000-0002-8890-077X>

References

1. M. Armand and J. M. Tarascon, "Building better batteries." *Nature*, **451**, 652 (2008).
2. Y. Liang, C.-Z. Zhao, H. Yuan, Y. Chen, W. Zhang, J.-Q. Huang, D. Yu, Y. Liu, M.-M. Titirici, and Y.-L. Chueh, "A review of rechargeable batteries for portable electronic devices." *InfoMat*, **1**, 6 (2019).
3. D. C. Brock and G. E. Moore, *Understanding Moore's Law: Four Decades of Innovation* (Chemical Heritage Foundation) (2006).
4. Z. Li, J. Huang, B. Yann Liaw, V. Metzler, and J. Zhang, "A review of lithium deposition in lithium-ion and lithium metal secondary batteries." *J. Power Sources*, **254**, 168 (2014).
5. X.-B. Cheng, R. Zhang, C.-Zi Zhao, and Q. Zhang, "Toward safe lithium metal anode in rechargeable batteries: a review." *Chem. Rev.*, **117**, 10403 (2017).

6. R. Zhang, N.-W. Li, X.-B. Cheng, Y.-X. Yin, Q. Zhang, and Y.-G. Guo, "Advanced micro/nanostructures for lithium metal anodes." *Advanced Science*, **4**, 1600445 (2017).
7. S. Li, J. Yang, and Y. Lu, "Lithium metal anode." *Encyclopedia of Inorganic and Bioinorganic Chemistry*, **1**.
8. W. Xu, J. L. Wang, F. Ding, X. L. Chen, E. Nasybutin, Y. H. Zhang, and J. G. Zhang, "Lithium metal anodes for rechargeable batteries." *Energy Environ. Sci.*, **7**, 513 (2014).
9. F. Orsini, A. D. Pasquier, B. Beaudoin, and J. M. Tarascon, "In situ scanning electron microscopy (sem) observation of interfaces with plastic lithium batteries." *J. Power Sources*, **76**, 19 (1998).
10. C. P. Nielsen and H. Bruus, "Morphological instability during steady electrodeposition at overlimiting currents." *Physical Review E*, **92**, 052310 (2015).
11. P. P. Natsiavas, K. Weinberg, D. Rosato, and M. Ortiz, "Effect of prestress on the stability of electrode-electrolyte interfaces during charging in lithium batteries." *Journal of the Mechanics and Physics of Solids*, **95**, 92 (2016).
12. C. Monroe and J. Newman, "The effect of interfacial deformation on electrodeposition kinetics." *J. Electrochem. Soc.*, **151**, A880 (2004).
13. A. Aryanfar, M. R. Hoffmann, and W. A. Goddard III, "Finite-pulse waves for efficient suppression of evolving mesoscale dendrites in rechargeable batteries." *Physical Review E*, **100**, 042801 (2019).
14. J. Steiger, D. Kramer, and R. Monig, "Mechanisms of dendritic growth investigated by in situ light microscopy during electrodeposition and dissolution of lithium." *J. Power Sources*, **261**, 112 (2014).
15. R. Younesi, G. M. Veith, P. Johansson, K. Edström, and T. Vegge, "Lithium salts for advanced lithium batteries: Li-metal, Li-O₂, and Li-S." *Energy Environ. Sci.*, **8**, 1905 (2015).
16. C. Brissot, M. Rosso, J. N. Chazalviel, and S. Lascaud, "In situ concentration cartography in the neighborhood of dendrites growing in lithium/polymer-electrolyte/lithium cells." *J. Electrochem. Soc.*, **146**, 4393 (1999).
17. A. Aryanfar, D. J. Brooks, A. J. Colussi, B. V. Merinov, W. A. Goddard III, and M. R. Hoffmann, "Thermal relaxation of lithium dendrites." *Phys. Chem. Chem. Phys.*, **17**, 8000 (2015).
18. R. Akolkar, "Modeling dendrite growth during lithium electrodeposition at sub-ambient temperature." *J. Power Sources*, **246**, 84 (2014).
19. Y. Yao, X. Zhao, A. A. Razzaq, Y. Gu, X. Yuan, R. Shah, Y. Lian, J. Lei, Q. Mu, and Y. Ma, "Mosaic rgo layer on lithium metal anodes for effective mediation of lithium plating and stripping." *Journal of Materials Chemistry A*, **7**, 12214 (2019).
20. J. Qian, Y. Li, M. Zhang, R. Luo, F. Wang, Y. Ye, Y. Xing, W. Li, W. Qu, and L. Wang, "Protecting lithium/sodium metal anode with metal-organic framework based compact and robust shield." *Nano Energy*, **60**, 866 (2019).
21. W. Deng, W. Zhu, X. Zhou, F. Zhao, and Z. Liu, "Regulating capillary pressure to achieve ultralow areal mass loading metallic lithium anodes." *Energy Storage Materials*, **23**, 693 (2019).
22. A. W. Abboud, E. J. Dufek, and B. Liaw, "Implications of local current density variations on lithium plating affected by cathode particle size." *J. Electrochem. Soc.*, **166**, A667 (2019).
23. C. Xu, Z. Ahmad, A. Aryanfar, V. Viswanathan, and J. R. Greer, "Enhanced strength and temperature dependence of mechanical properties of Li at small scales and its implications for Li metal anodes." *Proceedings of the National Academy of Sciences*, **114**, 57 (2017).
24. R. Bhattacharyya, B. Key, H. Chen, A. S. Best, A. F. Hollenkamp, and C. P. Grey, "In situ nmr observation of the formation of metallic lithium microstructures in lithium batteries." *Nat. Mater.*, **9**, 504 (2010).
25. S. Chandrashekar, N. M. Trease, H. J. Chang, L.-S. Du, C. P. Grey, and A. Jerschow, "7Li mri of li batteries reveals location of microstructural lithium." *Nat. Mater.*, **11**, 311 (2012).
26. Y. Li and Y. Qi, "Energy landscape of the charge transfer reaction at the complex li/sei/electrolyte interface." *Energy & Environmental Science*, **12**, 1286 (2019).
27. L. M. Kasmae, A. Aryanfar, Z. Chikneyan, M. R. Hoffmann, and A. J. Colussi, "Lithium batteries: Improving solid-electrolyte interphases via underpotential solvent electropolymerization." *Chem. Phys. Lett.*, **661**, 65 (2016).
28. J. L. Barton and J. O'M Bockris, "The electrolytic growth of dendrites from ionic solutions." *Proceedings of the Royal Society of London. Series A, Mathematical and Physical Sciences*, **268**, 485 (1962).
29. M. Z. Bazant, B. D. Storey, and A. A. Kornyshev, "Double layer in ionic liquids: overscreening vs crowding." *Phys. Rev. Lett.*, **106**, 046102 (2011).
30. V. Fleury, "Branched fractal patterns in non-equilibrium electrochemical deposition from oscillatory nucleation and growth." *Nature*, **390**, 145 (1997).
31. A. Aryanfar, D. Brooks, B. V. Merinov, W. A. Goddard III, A. J. Colussi, and M. R. Hoffmann, "Dynamics of lithium dendrite growth and inhibition: pulse charging experiments and monte carlo calculations." *The Journal of Physical Chemistry Letters*, **5**, 1721 (2014).
32. F. Ding, W. Xu, G. L. Graff, J. Zhang, M. L. Sushko, X. Chen, Y. Shao, M. H. Engelhard, Z. Nie, and J. Xiao, "Dendrite-free lithium deposition via self-healing electrostatic shield mechanism." *J. Am. Chem. Soc.*, **135**, 4450 (2013).
33. S. J. Harris, A. Timmons, D. R. Baker, and C. Monroe, "Direct in situ measurements of li transport in li-ion battery negative electrodes." *Chem. Phys. Lett.*, **485**, 265 (2010).
34. C. Brissot, M. Rosso, J. N. Chazalviel, and S. Lascaud, "Concentration measurements in lithium/polymer-electrolyte/lithium cells during cycling." *J. Power Sources*, **94**, 212 (2001).
35. P. Bai, J. Li, F. R. Brushett, and M. Z. Bazant, "Transition of lithium growth mechanisms in liquid electrolytes." *Energy & Environmental Science*, **9**, 3221 (2016).
36. G. Gonzalez, M. Rosso, and E. Chassaing, "Transition between two dendritic growth mechanisms in electrodeposition." *Physical Review E*, **78**, 011601 (2008).
37. C. M. Lopez, J. T. Vaughey, and D. W. Dees, "Morphological transitions on lithium metal anodes." *J. Electrochem. Soc.*, **156**, A726 (2009).
38. J. N. Chazalviel, "Electrochemical aspects of the generation of ramified metallic electrodeposits." *Phys. Rev. A*, **42**, 7355 (1990).
39. C. Monroe and J. Newman, "Dendrite growth in lithium/polymer systems—a propagation model for liquid electrolytes under galvanostatic conditions." *J. Electrochem. Soc.*, **150**, A1377 (2003).
40. T. A. Witten and L. M. Sander, "Diffusion-limited aggregation." *Phys. Rev. B*, **27**, 5686 (1983).
41. M. Zhang and C. Deng, "Fractal simulation of thin film nucleation growth process using a diffusion-limited aggregation model." *Modern Physics Letters B*, **32**, 1850408 (2018).
42. A. J. Bard and L. R. Faulkner, *Electrochemical Methods: Fundamentals and Applications* (Wiley, New York, NY) 2 ed., 1980 (1980).
43. D. Tewari and P. P. Mukherjee, "Mechanistic understanding of electrochemical plating and stripping of metal electrodes." *Journal of Materials Chemistry A*, **7**, 4668 (2019).
44. W. W. Mullins and R. F. Sekerka, "Morphological stability of a particle growing by diffusion or heat flow." *J. Appl. Phys.*, **34**, 323 (1963).
45. W. W. Mullins and R. F. Sekerka, "Stability of a planar interface during solidification of a dilute binary alloy." *J. Appl. Phys.*, **35**, 444 (1964).
46. J. W. Diggle, A. R. Despic, and J. O'M. Bockris, "The mechanism of the dendritic electrocrystallization of zinc." *J. Electrochem. Soc.*, **116**, 1503 (1969).
47. Z. Ahmad and V. Viswanathan, "Stability of electrodeposition at solid-solid interfaces and implications for metal anodes." *Phys. Rev. Lett.*, **119**, 056003 (2017).
48. J. Tan, A. M. Tartakovsky, K. Ferris, and E. M. Ryan, "Investigating the effects of anisotropic mass transport on dendrite growth in high energy density lithium batteries." *J. Electrochem. Soc.*, **163**, A318 (2015).
49. J. Tan and E. M. Ryan, "Computational study of electro-convection effects on dendrite growth in batteries." *Journal of Power Sources*, **323**, 67 (2016).
50. M. Z. Bazant, "Regulation of ramified electrochemical growth by a diffusive wave." *Physical Review E*, **52**, 1903 (1995).
51. R. Akolkar, "Mathematical model of the dendritic growth during lithium electrodeposition." *J. Power Sources*, **232**, 23 (2013).
52. C. Leger, J. Elezgaray, and F. Argoul, "Dynamical characterization of one-dimensional stationary growth regimes in diffusion-limited electrodeposition processes." *Physical Review E*, **58**, 7700 (1998).
53. C. Leger, J. Elezgaray, and F. Argoul, "Experimental demonstration of diffusion-limited dynamics in electrodeposition." *Phys. Rev. Lett.*, **78**, 5010 (1997).
54. C. Léger, J. Elezgaray, and F. Argoul, "Internal structure of dense electrodeposits." *Physical Review E*, **61**, 5452 (2000).
55. J.-H. Han, E. Khoo, P. Bai, and M. Z. Bazant, "Over-limiting current and control of dendritic growth by surface conduction in nanopores." *Sci. Rep.*, **4**, 7056 (2014).
56. R. Failla, M. Bologna, and B. Tellini, "Dendrite growth model in battery cell combining electrode edge effects and stochastic forces into a diffusion limited aggregation scheme." *Journal of Power Sources*, **433**, 126675 (2019).
57. G. Bucci and J. Christensen, "Modeling of lithium electrodeposition at the lithium/ceramic electrolyte interface: The role of interfacial resistance and surface defects." *Journal of Power Sources*, **441**, 227186 (2019).
58. D. A. Cogswell, "Quantitative phase-field modeling of dendritic electrodeposition." *Physical Review E*, **92**, 011301 (2015).
59. D. R. Ely, A. Jana, and R. E. García, "Phase field kinetics of lithium electrodeposits." *J. Power Sources*, **272**, 581 (2014).
60. K. Wang, Y. Xiao, P. Pei, X. Liu, and Y. Wang, "A phase-field model of dendrite growth of electrodeposited zinc." *J. Electrochem. Soc.*, **166**, D389 (2019).
61. A. Jana and R. E. García, "Lithium dendrite growth mechanisms in liquid electrolytes." *Nano Energy*, **41**, 552 (2017).
62. A. Jana, S. I. Woo, K. S. N. Vikrant, and R. E. García, "Electrochemomechanics of lithium dendrite growth." *Energy & Environmental Science*, **12**, 3595 (2019).
63. F. Hao, A. Verma, and P. P. Mukherjee, "Mechanistic insight into dendrite-sei interactions for lithium metal electrodes." *Journal of Materials Chemistry A*, **6**, 19664 (2018).
64. Aiping Wang, Sanket Kadam, Hong Li, Siqi Shi, and Yue Qi, "Review on modeling of the anode solid electrolyte interphase (sei) for lithium-ion batteries." *npj Computational Materials*, **4**, 1 (2018).
65. B. Horstmann, F. Single, and A. Latz, "Review on multi-scale models of solid-electrolyte interphase formation." *Current Opinion in Electrochemistry*, **13**, 61 (2019).
66. G. Liu and W. Lu, "A model of concurrent lithium dendrite growth, sei growth, sei penetration and regrowth." *J. Electrochem. Soc.*, **164**, A1826 (2017).
67. A. Maraschky and R. Akolkar, "Mechanism explaining the onset time of dendritic lithium electrodeposition via considerations of the Li⁺ transport within the solid electrolyte interphase." *J. Electrochem. Soc.*, **165**, D696 (2018).
68. A. Maraschky and R. Akolkar, "Temperature dependence of dendritic lithium electrodeposition: a mechanistic study of the role of transport limitations within the SEI." *J. Electrochem. Soc.*, **167**, 062503 (2020).
69. M. R. Hoffman, A. Aryanfar, K. Cho, C. A. Cid, D. Kwon, and Y. Qu, (2021) "Self-contained, pv-powered domestic toilet and wastewater treatment system." US Patent 10,981,811.
70. N. Otsu, "A threshold selection method from gray-level histograms." *Automatica*, **11**, 23 (1975).

71. A. Aryanfar, D. J. Brooks, A. J. Colussi, and M. R. Hoffmann, "Quantifying the dependence of dead lithium losses on the cycling period in lithium metal batteries." *Phys. Chem. Chem. Phys.*, **16**, 24965 (2014).
72. A. Bonnefont, F. Argoul, and M. Z. Bazant, "Analysis of diffuse-layer effects on time-dependent interfacial kinetics." *Journal of Electroanalytical Chemistry*, **500**, 52 (2001).
73. M. Z. Bazant, K. Thornton, and A. Ajdari, "Diffuse-charge dynamics in electrochemical systems." *Physical Review E*, **70** (2004).
74. P. Debye and E. Hückel, "On the theory of electrolytes. I. freezing point depression and related phenomena." *Phys. Z.*, **24**, 185 (1923).
75. B. J. Kirby, *Micro-and Nanoscale Fluid Mechanics: Transport in Microfluidic Devices* (Cambridge university press, Cambridge, UK) (2010).
76. D. Halliday, R. Resnick, and J. Walker, *Fundamentals of Physics* (Wiley, New York, NY) (2013).
77. National Institute of Standards and Technology. NIST Physics Laboratory, *The NIST Reference on Constants, Units and Uncertainty* (National Institute of standards and technology) (1998).
78. A. Manthiram, "Materials challenges and opportunities of lithium ion batteries." *The Journal of Physical Chemistry Letters*, **2**, 176 (2011).
79. A. Manthiram, K. Chemelewski, and E.-S. Lee, "A perspective on the high-voltage limn 1.5 ni 0.5 o 4 spinel cathode for lithium-ion batteries." *Energy & Environmental Science*, **7**, 1339 (2014).
80. W. Li, B. Song, and A. Manthiram, "High-voltage positive electrode materials for lithium-ion batteries." *Chem. Soc. Rev.*, **46**, 3006 (2017).
81. Grad Harold, "Principles of the kinetic theory of gases." In *Thermodynamik der Gase/Thermodynamics of Gases* (Springer, New York, NY) p. 205 (1958).
82. M. Roberts, P. Johns, J. Owen, D. Brandell, K. Edstrom, G. El Enany, C. Guery, D. Golodnitsky, M. Lacey, and C. Lecoer, "3d lithium ion batteries from fundamentals to fabrication." *Journal of Materials Chemistry*, **21**, 9876 (2011).
83. A. J. Bard, R. Parsons, and J. Jordan, *Standard Potentials in Aqueous Solution* (CRC press, New York, NY) 6 (1985).
84. W. M. Haynes, *Handbook of Chemistry & Physics* (Taylor and Francis, New York, NY) 93rd edn ed. (2012).
85. C. S. Helrich, *Modern Thermodynamics with Statistical Mechanics* (Springer, New York, NY) (2008).
86. A. Aryanfar, D. J. Brooks, T. Cheng, B. V. Merinov, W. A. Goddard, A. J. Colussi, and M. R. Hoffmann, "Three dimensional modeling of dendrite growth in rechargeable lithium metal batteries." *Meeting Abstracts, The Electrochemical Society*, **15**, 1154 (2015).
87. C. Brissot, M. Rosso, J. N. Chazalviel, and S. Lascaud, "Dendritic growth mechanisms in lithium/polymer cells." *J. Power Sources*, **81**, 925 (1999).
88. C. Brissot, M. Rosso, J. N. Chazalviel, P. Baudry, and S. Lascaud, "In situ study of dendritic growth in lithium/peo-salt/lithium cells." *Electrochim. Acta*, **43**, 1569 (1998).
89. M. Rosso, "Electrodeposition from a binary electrolyte: new developments and applications." *Electrochim. Acta*, **53**, 250 (2007).
90. H. J. S. Sand III, "On the concentration at the electrodes in a solution, with special reference to the liberation of hydrogen by electrolysis of a mixture of copper sulphate and sulphuric acid." *The London, Edinburgh, and Dublin Philosophical Magazine and Journal of Science*, **1**, 45 (1901).
91. R. N. Wasalathanthri and R. Akolkar, "Perspective: does the sand equation reliably predict the onset of morphological evolution in lithium electrodeposition?" *J. Electrochem. Soc.*, **169**, 092519 (2022).
92. V. Fleury, J.-N. Chazalviel, M. Rosso, and B. Sapoval, "The role of the anions in the growth speed of fractal electrodeposits." *J. Electroanal. Chem. Interfacial Electrochem.*, **290**, 249 (1990).
93. V. Fleury, J.-N. Chazalviel, and M. Rosso, "Theory and experimental evidence of electroconvection around electrochemical deposits." *Phys. Rev. Lett.*, **68**, 2492 (1992).
94. V. Fleury, J.-N. Chazalviel, and M. Rosso, "Coupling of drift, diffusion, and electroconvection, in the vicinity of growing electrodeposits." *Physical Review E*, **48**, 1279 (1993).